Scattering singularities of optical waveguides under complex modulation

Qingjie Liu,[1] Chengzhi Qin,[1] Bing Wang,[1,*] and Peixiang Lu[1,2,†]

[1]*School of Physics and Wuhan National Laboratory for Optoelectronics, Huazhong University of Science and Technology, Wuhan, 430074, China*

[2]*Hubei Key Laboratory of Optical Information and Pattern Recognition, Wuhan Institute of Technology, Wuhan, 430205, China*

(Received 14 November 2019; accepted 12 February 2020; published 16 March 2020)

We employ complex index modulation to manipulate light scattering in a waveguide and achieve different kinds of singularities in the system. The singularities refer to poles or zeros in the scattering and transfer matrices. By using spatially complex index modulation, we realize unidirectional zero-reflection singularities, which can be manipulated by adjusting the modulation phase difference between the real and imaginary parts. Laser-coherent perfect absorber singularities with both diverging reflectance and transmittance are also achieved by cascading two waveguides with different modulation phases. Meanwhile, bidirectional zero-reflection singularities with reflectionless light transporting on both sides of the waveguides are also demonstrated. In addition, we utilize temporally complex modulation to obtain transfer matrix singularities and achieve nonreciprocal light transmission. The study may find great applications in light amplification, attenuation, and absorption, as well as constructing nonreciprocal optical devices.

DOI: 10.1103/PhysRevA.101.033818

I. INTRODUCTION

Singularities manifest themselves as unique properties in non-Hermitian systems [1–5]. One representative example is the singularities in energy spectrum, i.e., the exceptional points (EPs), at which two branches of Riemann surface coalesce [6–10]. EPs have been explored to take on a variety of effects, such as band repulsion, crossing, bifurcation, and phase transition [11–13]. In a scattering system, EPs also appear when both the eigenvalues and eigenvectors of the scattering matrix coalesce. In this case, the system exhibits unidirectional or bidirectional invisibility, which refers to reflectionless light for either side incidence [7–9,14,15]. Another example is eigenvalue singularities, i.e., the poles and zeros of the scattering matrix eigenvalues [16–21]. These singularities also have physically observable effects: the poles of scattering matrix may lead to lasing as the system could generate outgoing waves without external inputs. On the contrary, the scattering matrix zeros correspond to coherent perfect absorption (CPA) as the system absorbs appropriate incoming waves perfectly without reflections, manifesting a time-reversal process of lasing. By engineering the laser-CPA singularities, a variety of phenomena can be readily observed, including super scattering [22] and power oscillation [23,24]. Moreover, near the laser-CPA singularities, the scattering structure is usually accompanied by giant light transmittance and reflectance, which can thus be exploited to manipulate light amplification, attenuation as well as absorption [20–22,25].

Most previous research on light scattering singularities focus on static structures where the refractive index distributions are constant, such as the realization of laser-CPA singularities in PT-symmetric structures [18,26,27]. In recent years, the index-modulated systems have attracted more attention, especially in the context of nonreciprocal light transmission [28,29] and chiral mode switches [30,31]. In terms of the modulation formats, index modulation can be divided into two groups: spatial modulation and temporal modulation. The spatial index modulation can impose a modulation wave vector into the structure and hence can arouse mode couplings with different wave vectors. In contrast, the temporal modulation can induce mode frequency shift and thus be exploited to achieve nonreciprocal light transmission. Specifically, the temporal modulation has been recently introduced in coupled resonators [32], Mathieu slab [33], and waveguides [34–37] where nonreciprocal gain or amplification and bidirectional invisibility have been realized. Thanks to the facility in controlling mode transitions, we are able to introduce modulation approaches to the scattering systems, aiming to provide more functionality to control light scattering properties.

In this work, we introduce both spatially and temporally complex modulations to a waveguide system and realize control over the singularities. First, spatially complex index modulation is applied on a single waveguide and the unidirectional zero-reflection singularities are realized, which manifest reflectionless light transmission. Then we utilize two cascaded waveguides with different modulation phases and realize the laser-CPA singularities showing giant transmission and reflectances as well as bidirectional reflectionless transmission. All these singularities can be readily controlled by the modulation phase difference of the two waveguides and waveguide length. Finally, the transfer matrix singularities

*wangbing@hust.edu.cn
†lupeixiang@hust.edu.cn

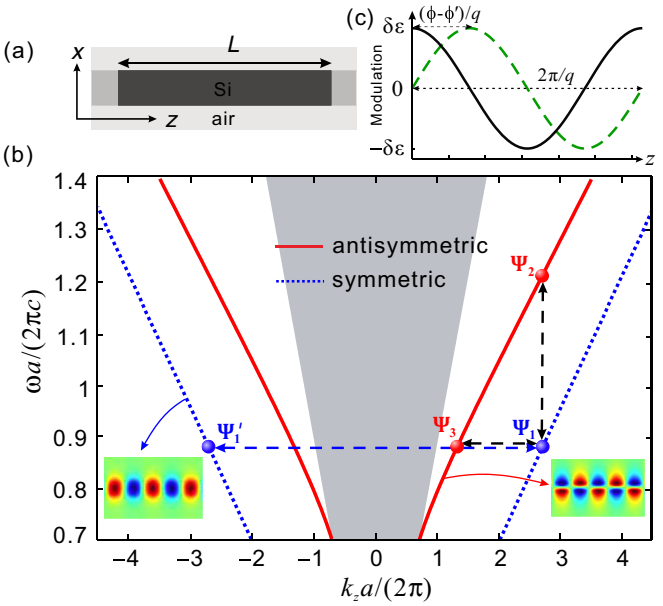

FIG. 1. (a) Schematic of a two-dimensional slab waveguide consisting of silicon core embedded in air cladding. (b) Waveguide dispersion diagram, where the solid red and dotted blue curves denote TE_0 and TE_1 bands, and the dark region represent the light cone. The frequencies and wave numbers of the modes Ψ_1, Ψ_1', Ψ_2, and Ψ_3 are $\omega_1 = \omega_1' = \omega_3 = 0.8879(2\pi c/a)$, $\omega_2 = 1.202(2\pi c/a)$ and $k_{z1} = k_{z2} = 2.716(2c/a)$, $k_{z3} = 1.366(2c/a)$, $k_{z1}' = -2.716(2c/a)$, where $a = 1\ \mu$m. (c) Spatial profiles of the real (black solid) and imaginary (green dashed) modulation functions.

in a waveguide under temporally complex modulation are discussed, where the nonreciprocal light transmission and mode conversion are observed.

II. RESULTS AND DISCUSSIONS

A. Spatially complex modulation

To start, we investigate light scattering properties in a waveguide undergoing spatially complex index modulation. The system structure is depicted in Fig. 1(a), which consists of a silicon slab waveguide with core permittivity $\varepsilon_d = 12.25$ and width $d = 0.22\ \mu$m imbedded in the air with permittivity $\varepsilon_0 = 1$. The central dark area represents the modulated region, of which the length is denoted by L. As shown by the dotted blue and solid red curves in Fig. 1(b), the waveguide can support symmetric (TE_0) and antisymmetric (TE_1) modes, respectively. In the presence of the permittivity modulation, photonic interband or intraband transitions will occur between the modes. First, we consider a spatially complex modulation of the core permittivity applied to the modulation region, of which the modulation profile reads

$$\varepsilon(z) = \varepsilon_d + \delta\varepsilon\cos(qz+\phi) + i\delta\varepsilon\cos(qz+\phi'), \tag{1}$$

where $\delta\varepsilon$ and q are common modulation amplitude and wavenumber, ϕ and ϕ' are modulation phases of the real and imaginary parts, respectively. The profiles of the real and imaginary modulations are plotted in Fig. 1(c), where we choose $q = k_{z1} - (-k_{z1}') = 2k_{z1}$, such that the phase-matching condition is satisfied between the forward and backward modes Ψ_1 and Ψ_1', giving rise to the coupling between them. The electric-field distribution in the modulated region is thus the superposition of Ψ_1 and Ψ_1', $E(x,z,t) = a_1(z)E_1(x)\ \exp[i(k_{z1}z-\omega_1 t)] + a_2(z)E_1(x)\ \exp[i(-k_{z1}z-\omega_1 t)]$, where $E_1(x)$ and $a_{1,2}(z)$ are the normalized mode profile and mode amplitudes, respectively. Using slowly-varying envelope approximation [28,29], we can obtain the coupled-mode equation

$$i\frac{d}{dz}\begin{bmatrix}a_1(z)\\ a_2(z)\end{bmatrix} = \mathbf{H}\begin{bmatrix}a_1(z)\\ a_2(z)\end{bmatrix} = \begin{bmatrix}-\frac{\delta\varepsilon}{2\pi}\alpha & -(Ce^{-i\phi}+iCe^{-i\phi'})\\ Ce^{i\phi}+iCe^{i\phi'} & \frac{\delta\varepsilon}{2\pi}\alpha\end{bmatrix}\begin{bmatrix}a_1(z)\\ a_2(z)\end{bmatrix}, \tag{2}$$

where $C = 1/2\varepsilon_0\omega_1\int\delta\varepsilon E_1^*(x)E_1(x)dx$ is the common coupling strength between Ψ_1 and Ψ_1' induced by the real and imaginary modulations, respectively. The diagonal term denotes the mode intrinsic loss, as described by $\alpha = \delta n k_{z1}$, where δn is the imaginary part of the effective index modulation amplitude [38]. The solution of Eq. (2) is $[a_1(z), a_2(z)]^{\mathrm{T}} = \mathbf{M}[a_1(0), a_2(0)]^{\mathrm{T}}$, where $\mathbf{M} = [M_{11}, M_{12}; M_{21}, M_{22}]$ is the mode transfer matrix, which is given by

$$\mathbf{M} = \frac{1}{B_- - B_+}\begin{bmatrix}B_-e^{-iE_+z} - B_+e^{-iE_-z} & -e^{-iE_+z} + e^{-iE_-z}\\ B_+B_-(e^{-iE_+z} - e^{-iE_-z}) & -B_+e^{-iE_+z} + B_-e^{-iE_-z}\end{bmatrix}, \tag{3}$$

in which the parameters are

$$E_\pm = \pm\sqrt{\left(\frac{\delta\varepsilon\cdot\alpha}{2\pi}\right)^2 - 2iC^2\cos(\phi-\phi')}, \tag{4}$$

$$B_\pm = \frac{-\frac{\delta\varepsilon\cdot\alpha}{2\pi} - E_\pm}{Ce^{i\phi}+iCe^{i\phi'}} = \frac{\left(-\frac{\delta\varepsilon\cdot\alpha}{2\pi} - E_\pm\right)e^{i(\phi+\phi'+\frac{\pi}{2})/2}}{2\cos\left(\phi-\phi'-\frac{\pi}{2}\right)}. \tag{5}$$

From the transfer matrix, we can obtain the scattering matrix $\mathbf{S} = [t_1, r_1; r_2, t_2]$, [5,39] with

$$r_1 = -\frac{M_{21}}{M_{22}},\quad r_2 = \frac{M_{12}}{M_{22}},\quad t_1 = \frac{1}{M_{22}},\quad t_2 = M_{11} - \frac{M_{12}M_{21}}{M_{22}}, \tag{6}$$

where $r_{1,2}$ and $t_{1,2}$ are the reflection and transmission coefficients from the left- and right-side incidences, respectively. It can be verified that $\det(\mathbf{M}) = 1$, such that $t_1 = t_2 = t = 1/M_{22}$. The mode reflectance and transmittance are thus given by $R_{1,2} = |r_{1,2}|^2$ and $T = |t|^2$.

Figure 2(a) shows the mode reflectances R_1, R_2 and transmittance T as functions of the modulation phase difference $\phi-\phi'$ between the real and imaginary modulations for different modulation lengths $L = \pi$ and $L = 2\pi$, respectively. For visualization purposes, the modulation amplitude is fixed at $\delta\varepsilon = 0.2$ such that the effect could be observed with a relatively short waveguide. Experimentally, the real and imaginary modulations may be

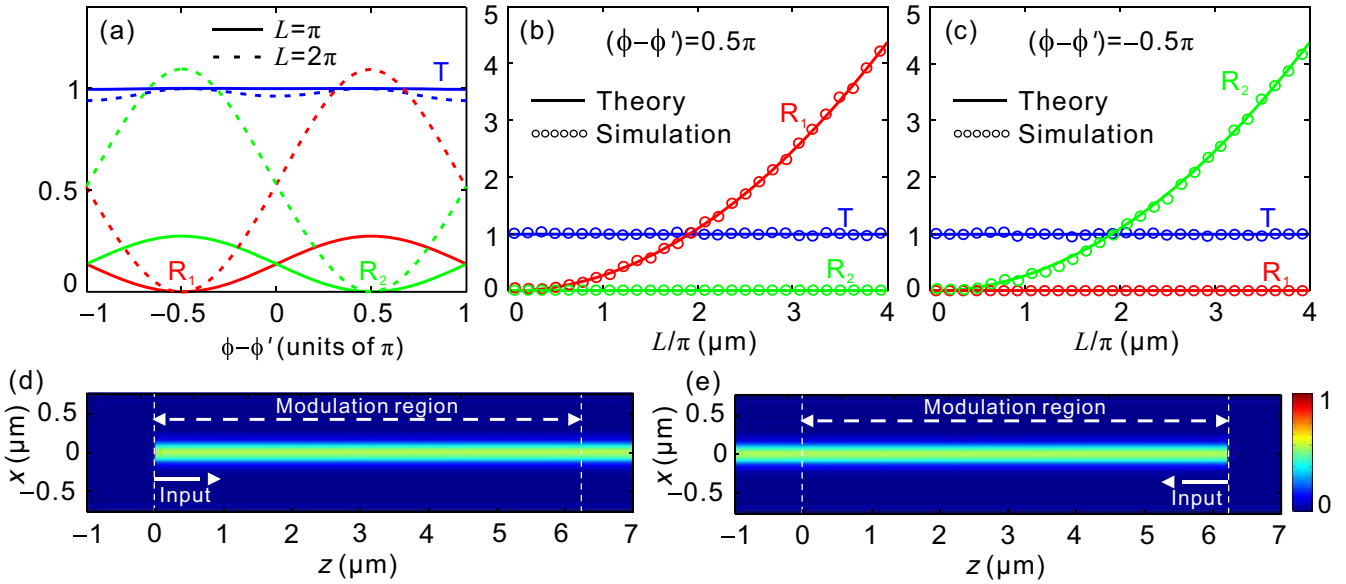

FIG. 2. (a) Left and right incidence reflectances R_1, R_2 and transmission T as functions of the modulation phase difference $\phi-\phi'$ between real and imaginary parts for different modulation lengths of $L=\pi$ and $L=2\pi$, respectively. (b),(c) Mode reflectance and transmittance as functions of the modulation lengths for fixed modulation phase differences $\phi-\phi'=\pm\pi/2$. The solid and circle curves represent the theoretical and simulated results, respectively. (d),(e) Electric-field distributions from the left incidence of Ψ_1 with $\phi-\phi'=-\pi/2$ and right incidence with $\phi-\phi'=\pi/2$. In (d) and (e), the white solid arrow indicates light incident direction and the while dashed arrow denotes the length of modulation region.

implemented by adding Si layers and Ge/Cr structures [38,40–42], respectively. The coupling strength and attenuation constant are calculated to be $C=0.0833\,\mu\mathrm{m}^{-1}$ and $\alpha=0.164\,\mu\mathrm{m}^{-1}$. For each choice of modulation length, there always exist two reflection singularities with $R_1=0$ at $\phi-\phi'=-\pi/2$ and $R_2=0$ at $\phi-\phi'=\pi/2$. Meanwhile, the transmittance goes to unity with $T=1$ at each singularity. Since the reflectance vanishes at each singularity, the system thus exhibits unidirectional invisibility or transparency [43,44], i.e., the mode incident from either side of the waveguide can transmit the modulated region without being reflected. More specifically, the eigenvalues and eigenvectors of the scattering matrix are simultaneously degenerate to $\lambda_s^{\pm}=t\pm(r_1r_2)^{1/2}=t$ and $[0,1]^{\mathrm{T}}$ at the singularities, manifesting the signature of EPs. In this regard, the EPs and the zero-reflection singularities can coincide with each other. Also note that the degenerate eigenvalue t is real, the mode thus exhibits no net energy amplification and dissipation in the modulation region. Figures 2(b) and 2(c) show the mode reflectance and transmittance as functions of the modulation length L at the two singularities of $\phi-\phi'=\pm\pi/2$. The theoretical results (solid curves) calculated from Eq. (6) agree well with numerical ones (circle curves) from finite-element simulations with COMSOL Multiphysics [45]. One sees that R_1 (R_2) increases monotonously while R_2 (R_1) $=0$ and $T=1$ keep unchanged as L increases. So in the vicinity of each singularity, the reflectance is insensitive to the change of waveguide parameter, indicating the robust reflection singularities. In Figs. 2(d) and 2(e), we simulate the electric-field evolutions at the singularities of $\phi-\phi'=\pm\pi/2$ and $L=2\pi$ by injecting the mode Ψ_1 from the left and right sides, respectively. In both cases, the mode can go through the modulated region with negligible reflectance, which further validates above theoretical analysis.

B. Spatially imaginary modulation

In this section, we further consider the situation where two cascaded modulation regions are included, as shown in Fig. 3(a). Specifically, we focus on a system where only the imaginary index modulation, i.e., gain-loss modulation is present. For the sake of simplicity, we consider the two regions have the same length L and attenuation constant α, each of which is modulated with a common modulation amplitude $\delta\varepsilon=0.2$ but different modulation phases ϕ_1' and ϕ_2'. The modulation profiles are illustrated in Fig. 3(b). In each region, the coupling matrix is given by

$$\mathbf{H}_{1,2}=\begin{bmatrix}-\frac{\delta\varepsilon}{2\pi}\alpha & -iCe^{-i\phi_{1,2}'}\\ iCe^{-i\phi_{1,2}} & \frac{\delta\varepsilon}{2\pi}\alpha\end{bmatrix},\tag{7}$$

each of which corresponds to a transfer matrix

$$\mathbf{M}_{1,2}=\frac{1}{B_--B_+}\begin{bmatrix}B_-e^{-iE_+z}-B_+e^{-iE_-z} & -e^{-iE_+z}+e^{-iE_-z}\\ B_+B_-(e^{-iE_+z}-e^{-iE_-z}) & -B_+e^{-iE_+z}+B_-e^{-iE_-z}\end{bmatrix},\tag{8}$$

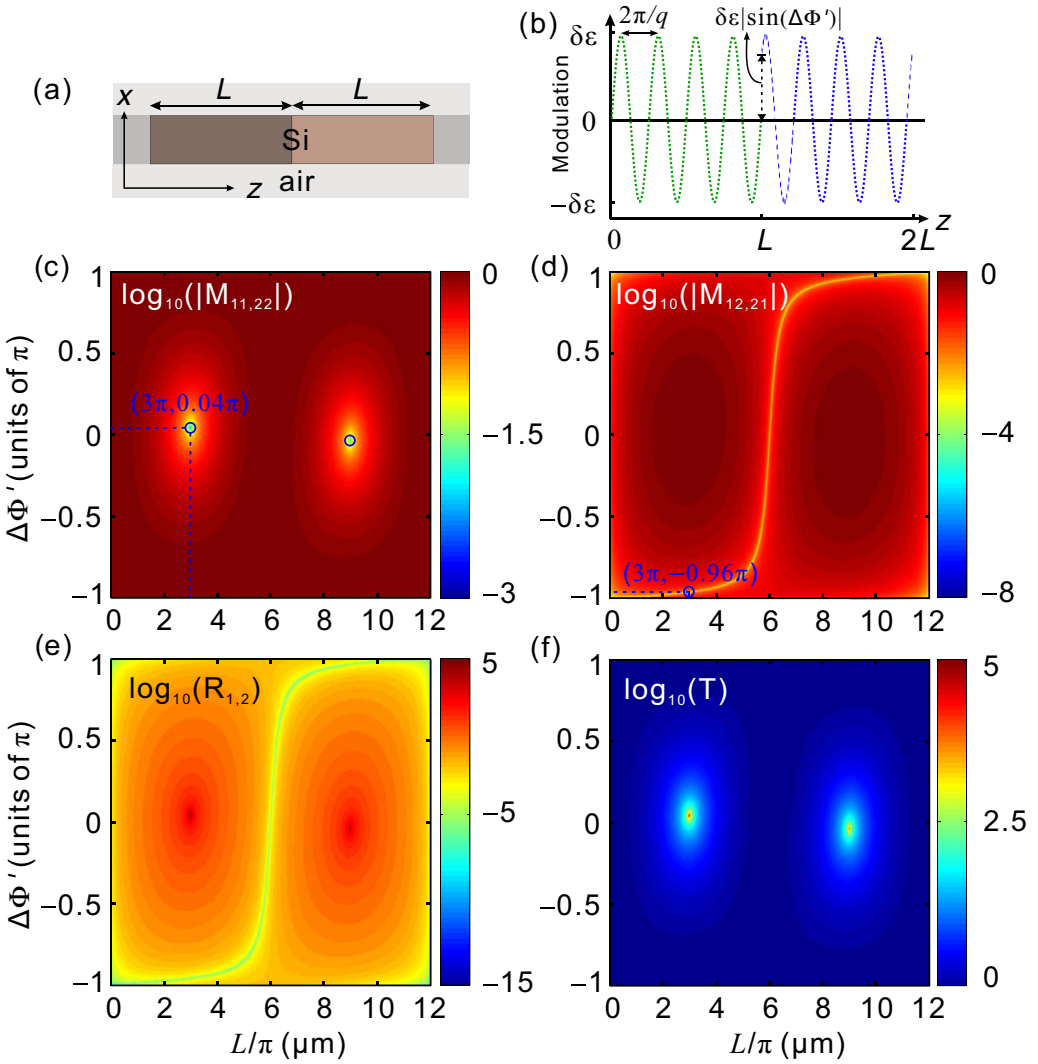

FIG. 3. (a) Schematic of the slab waveguide with two modulation regions. Each region has a length of L. (b) Spatial profiles of the real (black solid) and imaginary (green dashed and blue dashed) modulation functions. (c),(d) Theoretical transfer matrix elements $|M_{11,22}|$ and $|M_{12,21}|$. (e),(f) Mode reflectances $R_{1,2}$ and transmittance T as functions of the modulation phase difference $\Delta\phi' = \phi'_2 - \phi'_1$ in the two modulation regions and the modulation length L. The blue circles imply the singularities.

where

$$E_{\pm} = \pm\sqrt{\left(\frac{\delta\varepsilon\alpha}{2\pi}\right)^2 + C^2}, \tag{9}$$

$$B_{\pm} = -\frac{\frac{\delta\varepsilon\alpha}{2\pi} + E_{\pm}}{iCe^{i\phi'_{1,2}}}. \tag{10}$$

So the total mode transfer matrix is $\mathbf{M} = \mathbf{M}_2\mathbf{M}_1$. It can also be confirmed that $\det(\mathbf{M}) = 1$, and the matrix elements satisfy the following relation:

$$M_{11} = M^*_{22}, \quad M_{12} = -M^*_{21}. \tag{11}$$

So the reflectances from the left- and right-side incidences become equal to each other $R_1 = R_2 = R = |M_{12}|^2/|M_{22}|^2$, and $T = 1/|M_{22}|^2$. It is worth noting that the relation in Eq. (11) is different from that in PT-symmetric structure, $M_{12(21)} = -M^*{}_{12(21)}$ [18,46]. It will be discussed below that our structure shares some similarities compared to the PT-symmetric structures.

Figures 3(c)–3(f) show the logarithmic plot of the transfer matrix elements as functions of the length L and modulation phase difference $\Delta\phi' = \phi'_2 - \phi'_1$ between the two modulation regions. As shown in Fig. 3(c), there are two singularities with $|M_{11(22)}| = 0$ at $L = 3\pi$, $\Delta\phi' = 0.04\pi$ and $L = 9\pi$, $\Delta\phi' = -0.04\pi$. The variation of $|M_{12(21)}|$ is also depicted in Fig. 3(d), which possesses a pair of zeros. Since the two sets of zeros do not coincide with each other in positions, we can obtain both infinite reflectance and transmittance $R_1 = R_2 = |M_{12}|^2/|M_{22}|^2 = \infty$ and $T = 1/|M_{22}|^2 = \infty$ at the $|M_{11(22)}|$ zeros, as denoted in Figs. 3(e) and 3(f). The simultaneous infinite reflectance and transmittance means that the gain-loss modulated regions can generate outgoing waves without external input waves, corresponding to the laser operation conditions [16,19]. To gain more insight on the physical meaning of the $|M_{11(22)}|$ singularities, we also analyze the scattering

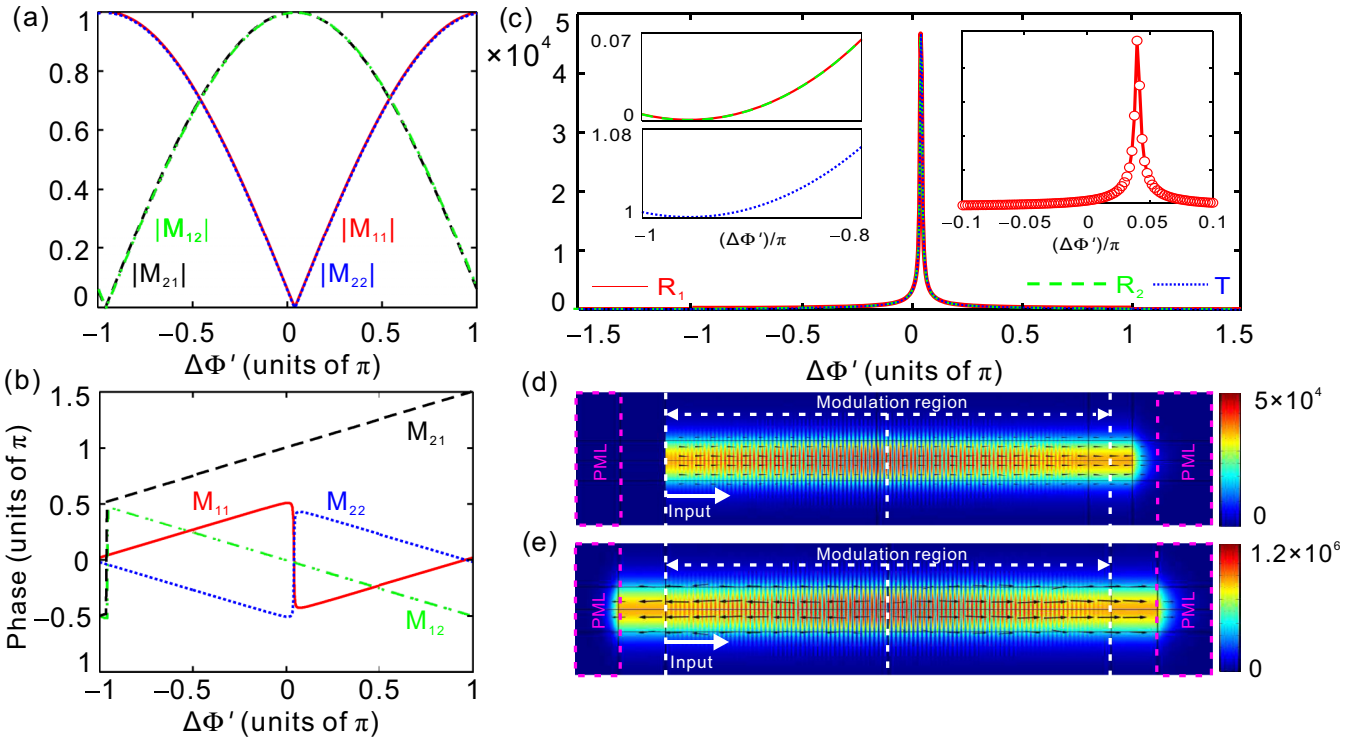

FIG. 4. (a),(b) Elements in the transfer matrix and (c) reflectances and transmission as functions of phase difference $\Delta\phi'$ with $L = 3\pi$. The solid and dashed curves show the theoretical results while the circles denote simulated results. (d),(e) Simulated electric field distribution in the waveguide as $R = 0$ in (d) and $R(T) = \infty$ in (e). The black arrows represent the direction of energy flow.

matrix eigenvalues. The two scattering matrix eigenvalues are $\lambda_s^{\pm} = t \pm (r_1 r_2)^{1/2}$, which constitute a nonunimodular inverse conjugate pair satisfying $\lambda_s^{\pm} = 1/(\lambda_s^{\mp})^*$. At the $|M_{11(22)}|$ zeros, we have $\lambda_s^+ = 0$ and $\lambda_s^- = \infty$, of which the former corresponds to the CPA, while the latter is a signature of the laser operation. Due to the simultaneous realization of CPA and laser, the system manifests itself as a CPA laser at the two zeros, which can be referred to laser-CPA singularities [18].

Then, we discuss the zero-reflection singularities (EP) $|M_{12(21)}| = 0$ at $L = 3\pi$, $\Delta\phi' = -0.96\pi$ as shown in Fig. 3(d). Since $M_{12} = M_{21} = 0$, we have $R_1 = R_2 = 0$, the system will manifest bidirectional invisibility, i.e., under the same parameters, the mode incident from either the left or right side of a waveguide can go through the modulated region without being reflected [33]. Note that bidirectional invisibility requires the simultaneous vanishing R_1 and R_2, which is different from the unidirectional invisibility case realized in Fig. 2(a), where either R_1 or R_2 vanishes but they cannot vanish simultaneously. At the singularities, we also have $T = 1$, meaning that there is no net energy amplification and dissipation in the modulation region from either left and right side incidences. It is also referred to the anisotropic transmission resonance satisfying $|T-1| = (R_1 R_2)^{1/2}$, as previously achieved in PT-symmetric structures [46]. In terms of the scattering matrix eigenvalues, they will become degenerate $\lambda_s^{\pm} = t \pm (r_1 r_2)^{1/2} = t$ at the bidirectional zero-reflection singularities.

In Figs. 4(a)–4(c), we choose a fixed modulation length $L = 3\pi$ and plot the transfer matrix elements, mode reflectance R_1 (or R_2) and transmittance T as the functions of the modulation phase difference $\Delta\phi' = \phi_2' - \phi_1'$ between the two modulation regions. It is shown in Fig. 4(a) that $|M_{11(22)}| = 0$ at $\Delta\phi' = 0.04\pi$. Meanwhile, as shown in the dotted blue and solid red curves in Fig. 4(b), $M_{11(22)}$ undergoes an abrupt phase jump at these laser/CPA singularities, which further validates the singularity nature for the zeros [14]. As shown by the dashed black and dashed dotted green curves in Fig. 4(b), this π-phase jump is also applicable to the bidirectional zero-reflection singularities with $|M_{12(21)}| = 0$. Figure 4(c) shows the mode reflectances and transmittance as functions of the modulation phase difference $\Delta\phi'$. The inset figures in Fig. 4(c) show both the minimum and maximum values of reflectance, corresponding to the bidirectional zero-reflection and laser-CPA singularities, respectively. In Figs. 4(d) and 4(e), we simulate the electric-field distributions at the bidirectional zero-reflection and laser-CPA singularities with $R_{1,2} = 0$ and $R_{1,2} = \infty$. Here the black arrows represent the direction of energy flow in the structure. For the zero-reflection singularity as shows in Fig. 4(d), the energy flow in the forward direction dominates while in the backward direction it is negligible. On the contrary, the energy flow in the backward direction dominates over that in the forward direction, as shown in Fig. 4(e), which is a clear signature for the laser-CPA singularity.

C. Temporally complex modulation

In above sections, we focus on spatial index modulation where the mode couplings between the forward and

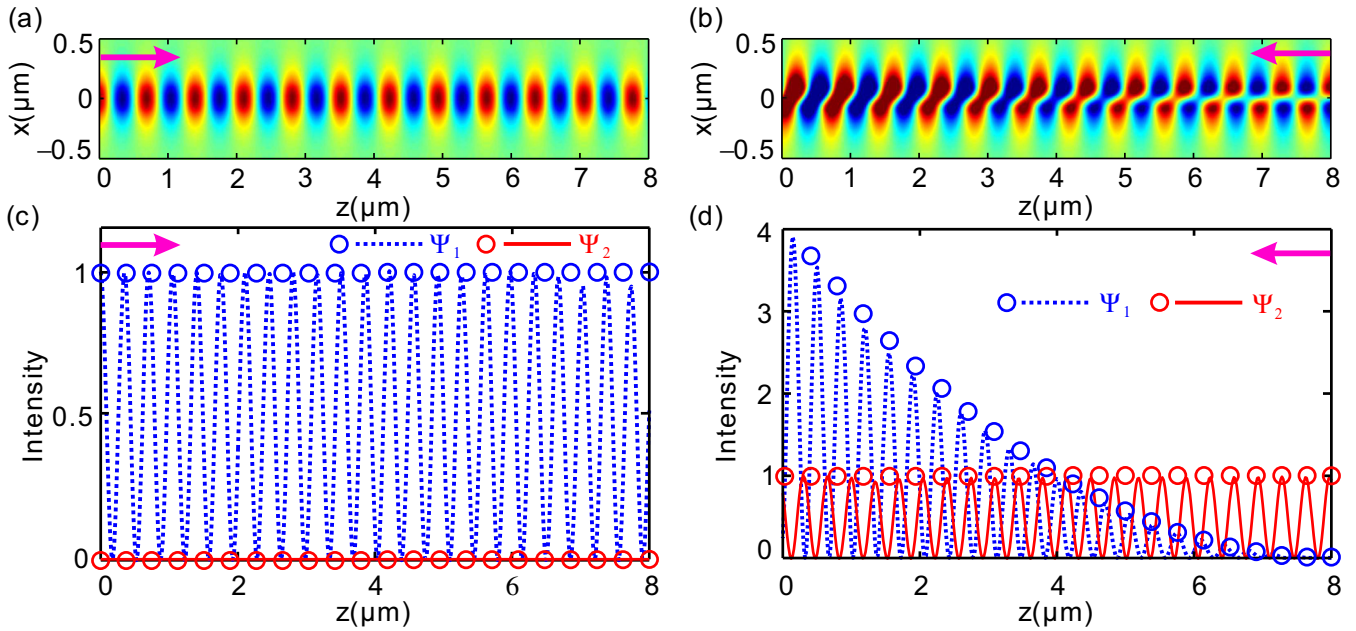

FIG. 5. (a),(b) Electric field E_z distribution in the x-z plane as Ψ_1 and Ψ_2 are injected in opposite directions. (c),(d) The profile and intensity of the modes propagating along the waveguide at $x = 0$. The circles denote the theoretical results of the mode intensities. The dashed and solid curves are simulated mode profiles. (c) and (d) are corresponding to (a) and (b), respectively.

backward propagating modes can be induced. In this section, we take a step further to study temporal index modulation and then realize nonreciprocal light propagation. It is interesting to compare the spatial and temporal index modulation: the former can induce the coupling between modes with same frequency but different wave vectors, while the later can arouse mode couplings with different frequencies but the same wave vectors. In this regard, the spatial modulation can be described by the scattering matrix, which is inapplicable for the temporal modulation [18,33,36]. However, both situations can be described by the mode transfer matrix. In this section, we investigate the singularities, i.e., the zeros in the transfer matrix elements for the temporal modulation and then exploit these singularities to achieve nonreciprocal light propagation. Specifically, we assume the waveguide core permittivity is subject to a temporally complex modulation

$$\varepsilon(x,t) = \varepsilon_d + \delta\varepsilon \mathrm{sgn}(x)\cos(\Omega t+\phi) + i\delta\varepsilon \mathrm{sgn}(x)\cos(\Omega t+\phi'), \tag{12}$$

where $\Omega = \omega_1 - \omega_2$ is chosen to match the frequency spacing between Ψ_1 and Ψ_2, which gives rise to the direct interband transitions between them [28,29]. Note that $\mathrm{sgn}(x)$ is a transverse modulation profile chosen to reach the maximum coupling strength. The corresponding coupled-mode equation reads

$$i\frac{d}{dz}\begin{bmatrix} a_1(z) \\ a_2(z) \end{bmatrix} = \begin{bmatrix} 0 & Ce^{-i\phi} + iCe^{-i\phi'} \\ Ce^{i\phi} + iCe^{i\phi'} & 0 \end{bmatrix}\begin{bmatrix} a_1(z) \\ a_2(z) \end{bmatrix}. \tag{13}$$

The solution can also be expressed by mode transfer matrix $\mathbf{M} = [M_{11}, M_{12}; M_{21}, M_{22}]$. Based on this, we can then define the mode conversion efficiency $|M_{i,j}|^2 (i, j = 1, 2)$, indicating the intensity ratio between the output mode Ψ_i to the incident Ψ_j, which reads

$$\begin{aligned} |M_{11}|^2 &= |M_{22}|^2 = \frac{e^{2\eta}}{4} + \frac{e^{-2\eta}}{4} + \cos^2(\eta) - \frac{1}{2}, \\ |M_{12}|^2 &= \sqrt{\frac{1-\sin(\phi-\phi')}{1+\sin(\phi-\phi')}}\left(\frac{e^{2\eta}}{4} + \frac{e^{-2\eta}}{4} - \cos^2(\eta) + \frac{1}{2}\right), \\ |M_{21}|^2 &= \sqrt{\frac{1+\sin(\phi-\phi')}{1-\sin(\phi-\phi')}}\left(\frac{e^{2\eta}}{4} + \frac{e^{-2\eta}}{4} - \cos^2(\eta) + \frac{1}{2}\right), \end{aligned} \tag{14}$$

where $\eta = Cz[\cos(\phi-\phi')]^{1/2}$. In general, for $\phi-\phi' \neq n\pi (n \in Z)$, we can obtain $|M_{12}| \neq |M_{21}|$, which indicates the nonreciprocal frequency conversion between the two modes: when Ψ_1 is incident from the left side, the intensity of output mode Ψ_2 ($|M_{21}|^2$) will be different from the intensity of output Ψ_1 ($|M_{12}|^2$) as Ψ_2 is incident from the right side. Specifically, for $\phi-\phi' = -\pi/2$, we have $\eta = 0$, $|M_{11}| = |M_{22}| = 1$, $|M_{12}| = 2Cz$, and $|M_{21}| = 0$. In the forward and backward directions, the antisymmetric mode Ψ_2 will convert to the symmetric mode Ψ_1, while the inverse conversion process is inhibited. For $\phi-\phi' = \pi/2$, we have $\eta = 0$, $|M_{11}| = |M_{22}| = 1$, $|M_{12}| = 0$ and $|M_{21}| = 2Cz$, thus Ψ_1 will convert to Ψ_2 and the inverse conversion process is inhibited. The phase differences $\phi-\phi' = \pm\pi/2$ correspond to the singularities in Eq. (14), manifesting the one-way nonreciprocal conversion.

The one-way nonreciprocal conversion between modes Ψ_1 and Ψ_2 can also be verified by COMSOL Multiphysics [45]. Figure 5 shows the distribution of electric field E_z and the corresponding relative intensity of two modes when Ψ_1 or Ψ_2 is injected. The phase difference is set as $\phi-\phi' = -\pi/2$. As

we input a Gaussian pulse in the symmetric mode Ψ_1, shown in Fig. 5(a), the field is uniform along the z direction without mode conversion. The intensity of Ψ_1 keeps invariable while Ψ_2 keeps zero, plotted in Fig. 5(c). As the antisymmetric mode Ψ_2 is injected from the right side, mode conversion happens, shown in Figs. 5(b)–5(d). The intensities of $\Psi_1(z)$ and $\Psi_2(z)$ calculated by simulated results (solid and dashed curves) are consistent with the analytical results (circles) by Eq. (14).

Thus we have realized the nonreciprocal frequency conversion, which cannot be achieved in a single waveguide under just real modulation. For the structure without gain-loss modulation, it needs at least two segments and a central unmodulated region having a width different from the modulated waveguides to realize the nonreciprocity property [29]. It should be mentioned that the nonreciprocity will disappear once the temporal modulation is changed to spatial modulation, for example, the conversion between Ψ_1 and Ψ_3 in Fig. 1(b). The coupled-mode equation and the corresponding transfer matrix are not altered as shown in Eqs. (13) and (14). The difference is that the modulation phases ϕ and ϕ' will reverse sign as the propagation direction is changed in the spatially modulated waveguide. For example, as Ψ_1 is incident from the left side, the amplitude of output Ψ_3 will be $|M_{21}(\phi, \phi')|$. As Ψ_3 is incident from the right side, the intensity of output Ψ_1 will be $|M_{12}(-\phi, -\phi')|$. According to Eq. (14), we can get that $|M_{21}(\phi, \phi')| = |M_{12}(-\phi, -\phi')|$, meaning a reciprocal conversion.

III. CONCLUSIONS

In summary, we have investigated the singularities of scattering and transfer matrices for light propagating in optical waveguides under spatial and temporal modulations. For spatial modulation applied on the waveguide, the unidirectional invisibility is realized at the singularity of EP. The reflectance along the opposite direction of propagation vanishes and the transmission becomes unitary. Bidirectional invisibility can also be achieved by modulating two regions of the waveguide. The reflectance on both directions becomes zero. Meanwhile, giant reflectance and transmission are realized at the singularities of laser and CPA. For temporal modulation, the one-way and nonreciprocal frequency conversion is realized at the singularity of transfer matrix, which is controllable by adjusting the modulation length and phase. The study provides a promising approach for manipulating light amplification, attenuation, and absorption, and possibility for nonreciprocal optical devices, such as optical isolators.

ACKNOWLEDGMENTS

The work is supported by National Natural Science Foundation of China (Grant No. 11674117, No. 11974124, No. 11947209), National Postdoctoral Program for Innovative Talent (Grant No. BX20190129) and Chinese Postdoctoral Science Foundation General Program (Grant No. 2019M660180).

Q.L. and C.Q. contributed equally to this work.

[1] Mostafazadeh, Phys. Rev. A **83**, 045801 (2011).
[2] Mostafazadeh, Phys. Rev. Lett. **102**, 220402 (2009).
[3] R. Aalipour, Phys. Rev. A **90**, 013820 (2014).
[4] S. Longhi, Phys. Rev. A **81**, 022102 (2010).
[5] Y. Li and C. Argyropoulos, Phys. Rev. B **99**, 075413 (2019).
[6] Y. Huang, Y. Shen, C. Min, S. Fan, and G. Veronis, Nanophotonics **6**, 977 (2017).
[7] M. Kang, H.-X. Cui, T.-F. Li, J. Chen, W. Zhu, and M. Premaratne, Phys. Rev. A **89**, 065801 (2014).
[8] L. Feng, X. Zhu, S. Yang, H. Zhu, P. Zhang, X. Yin, Y. Wang, and X. Zhang, Opt. Express **22**, 1760 (2014).
[9] Q. Liu, B. Wang, S. Ke, H. Long, K. Wang, and P. Lu, Opt. Express **25**, 7203 (2017).
[10] H. Cui, X. Cao, M. Kang, T. Li, M. Yang, T. Guo, Q. Guo, and J. Chen, Opt. Express **21**, 13368 (2013).
[11] X. Yin and X. Zhang, Nat. Mater. **12**, 175 (2013).
[12] W. D. Heiss, J. Phys. Math. Gen. **37**, 2455 (2004).
[13] W. D. Heiss, Phys. Rev. E **61**, 929 (2000).
[14] Y. Huang, G. Veronis, and C. Min, Opt. Express **23**, 29882 (2015).
[15] Y. Shen, X. Deng, and L. Chen, Opt. Express **22**, 19440 (2014).
[16] Y. D. Chong, L. Ge, and A. D. Stone, Phys. Rev. Lett. **106**, 093902 (2011).
[17] S. Longhi and L. Feng, Opt. Lett. **39**, 5026 (2014).
[18] S. Longhi, Phys. Rev. A **82**, 031801(R) (2010).
[19] Y. D. Chong, L. Ge, H. Cao, and A. D. Stone, Phys. Rev. Lett. **105**, 053901 (2010).
[20] Y. Sun, W. Tan, H.-q. Li, J. Li, and H. Chen, Phys. Rev. Lett. **112**, 143903 (2014).
[21] S. Longhi, Opt. Lett. **40**, 1278 (2015).
[22] S. Feng, Opt. Express **24**, 1291 (2016).
[23] S. Longhi, Phys. Rev. Lett. **105**, 013903 (2010).
[24] J. Tan, Y. Zhou, Q. Ke, M. He, J. Liang, Y. Li, M. Li, and P. Lu, Phys. Rev. A **101**, 013407 (2020).
[25] X. Huang, Q. Zhang, S. Xu, X. Fu, X. Han, W. Cao, and P. Lu, Opt. Express **27**, 38116 (2019).
[26] P. Meng, D. Zhao, D. Zhong, and W. Liu, Opt. Quantum Electron. **51**, 156 (2019).
[27] Q. Liu, S. Ke, and W. Liu, Opt. Quant. Electron. **50**, 356 (2018).
[28] Z. Yu and S. Fan, Nat. Photonics **3**, 91 (2009).
[29] K. Fang, Z. Yu, and S. Fan, Phys. Rev. Lett. **108**, 153901 (2012).
[30] J. Doppler, A. A. Mailybaev, J. Böhm, U. Kuhl, A. Girschik, F. Libisch, T. J. Milburn, P. Rabl, N. Moiseyev, and S. Rotter, Nature (London) **537**, 76 (2016).
[31] H. Xu, D. Mason, L. Jiang, and J. G. E. Harris, Nature (London) **537**, 80 (2016).
[32] T. T. Koutserimpas and R. Fleury, Phys. Rev. Lett. **120**, 087401 (2018).
[33] T. T. Koutserimpas, A. Alù, and R. Fleury, Phys. Rev. A **97**, 013839 (2018).
[34] A. Y. Song, Y. Shi, Q. Lin, and S. Fan, Phys. Rev. A **99**, 013824 (2019).
[35] S. Ke, D. Zhao, J. Liu, Q. Liu, Q. Liao, B. Wang, and P. Lu, Opt. Express **27**, 13858 (2019).

[36] C. Qin, Y. Peng, Y. Li, X. Zhu, B. Wang, C.-W. Qiu, and P. Lu, Phys. Rev. Appl. **11**, 064012 (2019).
[37] H. Chen, C. Qin, B. Wang, and P. Lu, Opt. Lett. **44**, 363 (2019).
[38] L. Feng, Y.-L. Xu, W. S. Fegadolli, M.-H. Lu, J. E. B. Oliveira, V. R. Almeida, Y.-F. Chen, and A. Scherer, Nat. Mater. **12**, 108 (2012).
[39] M. Kang, W. Zhu, H. Wang, and M. Premaratne, Opt. Express **25**, 18265 (2017).
[40] L. Feng, M. Ayache, J. Huang, Y.-L. Xu, M.-H. Lu, Y.-F. Chen, Y. Fainman, and A. Scherer, Science **333**, 729 (2011).
[41] H. Lira, Z. Yu, S. Fan, and M. Lipson, Phys. Rev. Lett. **109**, 033901 (2012).
[42] M. Ma, J. Wu, Y. Ning, F. Zhou, M. Yang, X. Zhang, J. Zhang, and G. Shang, Opt. Express **21**, 10335 (2013).
[43] Z. Lin, H. Ramezani, T. Eichelkraut, T. Kottos, H. Cao, and D. N. Christodoulides, Phys. Rev. Lett. **106**, 213901 (2011).
[44] S. Longhi, J. Phys. A. **44**, 485302 (2011).
[45] COMSOL Multiphysics, http://www.comsol.com.
[46] L. Ge, Y. D. Chong, and A. D. Stone, Phys. Rev. A **85**, 023802 (2012).